Analysis of Oscillation Frequency Deviation in Elastic Coupling Digital Drive System and Robust Notch Filter Strategy

Chen, Yangyang; Yang, Ming; Long, Jiang; Hu, Kun; Xu, Dianguo; Blaabjerg, Frede

Published in:
I E E E Transactions on Industrial Electronics

DOI (link to publication from Publisher):
10.1109/TIE.2018.2825300

Publication date:
2019

Document Version
Accepted author manuscript, peer reviewed version

Analysis of Oscillation Frequency Deviation in Elastic Coupling Digital Drive System and Robust Notch Filter Strategy

Yangyang Chen, Ming Yang, *Member, IEEE*, Jiang Long, Kun Hu, Dianguo Xu, *Fellow, IEEE*, and Frede Blaabjerg, *Fellow, IEEE*

***Abstract*—Mechanical resonance is a common problem in drive systems with elastic coupling. On-line adaptive notch filter is widely used to make system stable and the key of this method is to identify natural torsional frequency from speed feedback signal. However, because of common adoption of digital control and expansion of system bandwidth, oscillation frequency of the system is more likely to deviate from natural torsional frequency to a higher one. When oscillation frequency is shifted, the enabled notch filter with erroneous notch frequency causes an oscillation with a lower frequency and even makes resonance severer. In order to explain this phenomenon, the classical two-mass model based classification of resonances is checked at first. Then, by taking digital control, current loop delay and saturation nonlinearity into consideration, an improved digital mechanical resonance model is proposed and a criterion for oscillation frequency deviation is finally obtained. Furthermore, a more widely applicable and robust notch filter tuning strategy with no oscillation rebound is presented. In the end, the validity of aforementioned analysis and strategy is verified by experimental results.**

***Index Terms*—Two-mass system, mechanical resonance, digital control, notch filter.**

I. Introduction

ELASTIC joint like shaft, gear, ball-screw, timing-belt and coupling, is an essential part in industrial applications such as factory automation, computer numerical control machine tools, and industrial manipulators. Although elastic joint is cost-effective and flexible, it causes mechanical resonance and even leads to equipment damage [1]-[3]. Due to the market competition, companies prefer the controller with high gains parameters to improve production efficiency. However, with higher gains controllers are more likely to cause system instability and excite resonance, especially in flexible transmission system. Hence, guaranteeing the stability of the system is the precondition for improving the performance.

Manuscript received November 08, 2017; revised February 14, 2018; accepted March 16, 2018. This work was supported in part by the National Natural Science Foundation of China (51690182) and by the National Key Research and Development Program of China (2017YFB1300801).

Y. Chen, M. Yang, J. Long, K. Hu, and D. Xu are with the School of Electrical Engineering and Automation, Harbin Institute of Technology, Harbin 150001, China (e-mail: yangming_hit@163.com).

F. Blaabjerg is with the Department of Energy Technology, Aalborg University, Aalborg 9220, Denmark (e-mail: fbl@et.aau.dk).

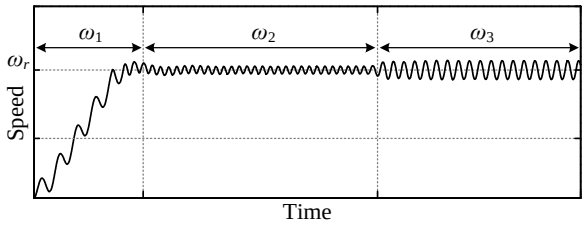

Fig. 1. Phenomenon of mechanical oscillation frequency deviation.

Hardware solutions such as increasing the stiffness coefficient of elastic joint, adding passive damping into system and choosing actuator with suitable inertia are most direct methods, but not economical. Thus, companies tend to modify controller and algorithm to make up for mechanical deficiencies and optimize the performance of in-use equipments. Suppression methods for mechanical resonance can be mainly divided into four groups:

1) Filter strategies: adding a low-pass or notch filter to conventional speed control structure to damp resonance-frequency component and compensate for the phase lag. Then, modified frequency-domain characteristics make system stable [1],[4]-[8].
2) Input shaping methods: correcting input reference and using iterative learning control in industrial assembly line with repeated tasks, which can suppress terminal vibration and make trajectory smooth [1],[9].
3) State variable measurement and estimation: using sensors or observers to achieve additional feedback or feedforward from one or more selected state variables to improve system characteristics and performances [10]-[13].
4) Modern control theories: utilizing predictive, adaptive, fuzzy, neural, and other modern control theories in two-mass system to cover the shortage of classical control strategies and enhance robustness of systems [14]-[22].

Among those methods, the filter strategies are more convenient for operation and easier to be achieved in digital controller, and notch filter based resonance damping is one of the most widely used methods. In conventional on-line adaptive notch filter (OANF), Fast Fourier Transformation is used to identify the resonance frequency ω_{NTF} (Natural Torsional Frequency) of the system from speed error signal in order to set the notch frequency. This method can complete the tuning of parameters and make system return to stability in a short time [4]-[7]. However, OANF still has some limitations in some cases that can be shown in Fig. 1. When speed feedback of the system is close to reference ω_r, an oscillation (frequency is ω_2,

$\omega_2>\omega_{NTF}$) appears. After adding a notch filter with notch frequency as ω_2, the resonance frequency shifts to ω_3 ($\omega_{NTF}<\omega_3<\omega_2$) and the resonance amplitude may become even larger, which does not satisfy the expectation. Although iterative tuning of notch frequency may possibly stabilize the system, this process is slow and not smooth enough. Hence, a more widely applicable and effective robust notch filter strategy with no oscillation rebound is needed.

In this paper, motivated by the above observations, a classification, based on traditional model, of mechanical resonances in transient and steady state has been done at first. Due to the limitation of traditional model, the self-sustained oscillation cannot be described clearly. Thus, an improved digital drive mechanical resonance model is built up to explain this type of oscillation. In the modeling process, some theories in LCL filter resonance are adopted [23]-[25]. Based on this improved model, a criterion for oscillation frequency deviation is obtained and a conclusion is drawn that choosing ω_{NTF} as notch frequency is more effective. In order to expand the applicable range of notch filter, a robust on-line adaptive notch filter (ROANF) is proposed. Adjustments of sampling period and output limit of speed loop are used to guarantee robust and smooth resonance suppression performance of ROANF. The effectiveness of the proposed model and strategy is verified on a 750W PMSM drive platform with elastic couplings.

II. Classical Mechanical Resonance Model and Resonance Frequency Classification

A. Two-Mass Model

Fig. 2 is a classical schematic for two-mass model. An elastic coupling is used to connect the motor and the actuator, whose stiffness is K_s and damping is C_w. J_m and J_l represent the inertia of motor and load respectively. Speed of motor ω_m is dependent on electromagnetic torque T_e and shaft torque T_s. Load torque T_l and T_s act together on the actuator, deciding its speed ω_l. Due to the fact that ω_m may be inconsistent with ω_l, there is an angle difference θ_s between motor angle θ_m and load angle θ_l. This deformation θ_s of the shaft is the cause of T_s.

Kinematics equations of the system are illustrated as follows

$$\begin{cases} J_m\dot{\omega}_m = T_e - T_s \\ J_l\dot{\omega}_l = T_s - T_l \\ T_s = C_w\left(\dot{\theta}_m - \dot{\theta}_l\right) + K_s\left(\theta_m - \theta_l\right) \\ \omega_m = \dot{\theta}_m \\ \omega_l = \dot{\theta}_l \end{cases} \tag{1}$$

The torque generated by the SPMSM is given by

$$T_e = 1.5p\left[\psi_f i_q + \left(L_d - L_q\right)i_d i_q\right] = 1.5p\psi_f i_q = K_t i_q \tag{2}$$

in which p is the pole pair number, ψ_f is the flux produced by the rotor magnet, $L_{d,q}$ and $i_{d,q}$ are the equivalent inductances and currents in the direction of the magnet flux and the quadrature direction, and K_t is the torque coefficient. Considering i_q is easier to detect than T_e in experiment and there is a proportional relationship between these two values, i_q is chosen as a representation of torque in the follow-up analysis. The nominal current i_{qN} corresponds to the nominal torque T_{eN} of the motor.

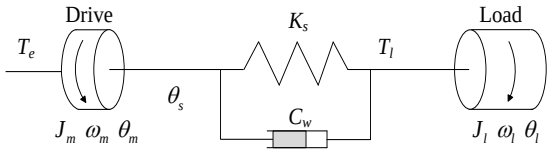

Fig. 2. Model of two-mass system.

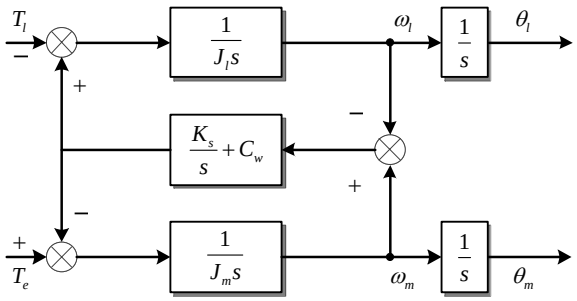

Fig. 3. Control diagram of two-mass system.

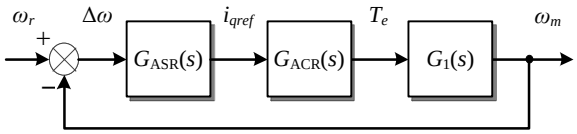

Fig. 4. Control diagram of classical two-mass drive system.

Then, the control diagram of two-mass system can be obtained as Fig. 3. Because C_w is small in most industrial systems, it is neglected in the following analysis. Hence, the transfer function of ω_m and T_e can be deduced as

$$G_1(s) = \frac{\omega_m}{T_e} = \frac{1}{(J_m + J_l)s}\frac{J_l s^2 + K_s}{\frac{J_m J_l}{(J_m + J_l)}s^2 + K_s} \tag{3}$$

Furthermore, natural torsional frequency ω_{NTF} and anti-resonance frequency ω_{ARF} of system are defined as

$$\omega_{NTF} = \sqrt{(J_m + J_l)K_s / \left(J_m J_l\right)} \qquad \omega_{ARF} = \sqrt{K_s / J_l} \tag{4}$$

B. Classification of Mechanical Resonance Frequency

In order to analyze the frequency of mechanical resonance, the model of the controller is also necessary besides the kinematics equation (3). Considering the bandwidth of current loop is much higher than that of speed loop, the torque coefficient K_t is preferably used to represent the current loop $G_{ACR}(s)$ in classical mechanical resonance model. On the other hand, influence of the integral term in speed loop controller $G_{ASR}(s)$ on the system concentrates on low frequency band far below ω_{NTF} in industrial applications. Considering this paper focuses on phase characteristics near ω_{NTF}, hence, only the proportional gain K_p is used to replace $G_{ASR}(s)$ and the integral part is ignored. To sum up, the control diagram of classical two-mass drive system can be shown as Fig. 4 in which i_{qref} is the output of the speed loop controller. Next, the following discusses the mechanical resonance frequency under transient and steady state of the classical mechanical resonance model.

1) Transient State

From Fig. 3, transfer function from T_l to ω_m can be given as

$$G_2(s) = \frac{\omega_m}{T_l} = \frac{-K_s}{J_m J_l s^3 + \left(J_m - J_l\right)K_s s} \tag{5}$$

This article has been accepted for publication in a future issue of this journal, but has not been fully edited. Content may change prior to final publication. Citation information: DOI 10.1109/TIE.2018.2825300, IEEE Transactions on Industrial Electronics

By combining (3) and (5), the unit step response of ω_m in the s-domain can be expressed as

$$\omega_m(s) = G_1(s)T_e(s) - G_2(s)T_l(s) = \frac{1}{J_m + J_l}\left(\frac{T_e(s) - T_l(s)}{s} + \frac{\left(J_l T_e(s) - J_m T_l(s)\right)s}{J_m\left(s^2 + \omega_{\mathrm{NTF}}^2\right)}\right) \quad (6)$$

Using inverse Laplace transform to rewrite (6), the unit step response expression of ω_m in the time domain can be written as

$$\omega_m(t) = \underbrace{\frac{T_e - T_l}{J_m + J_l}t}_{\text{ramp component}} + \underbrace{\frac{J_l T_e - J_m T_l}{J_m \omega_{\mathrm{NTF}}}\sin\left(\omega_{\mathrm{NTF}} t\right)}_{\text{resonance component}} \quad (7)$$

According to (7), in transient state when tracking the step reference, the ramp response of the drive system with elastic coupling contains a resonance component whose frequency is ω_{NTF}. The magnitude of this resonance component is inversely proportional related to frequency and independent with T_l.

2) Steady State

In dual closed loop drive system, once the speed feedback reaches the vicinity of the reference, speed loop recovers from saturation and continues to function. According to Fig. 4, the closed loop transfer function $G_c(s)$ can be expressed as

$$G_c(s) = G_{\mathrm{ASR}}(s)G_{\mathrm{ACR}}(s)G_1(s)\Big/\left[1 + G_{\mathrm{ASR}}(s)G_{\mathrm{ACR}}(s)G_1(s)\right] = \frac{K_p K_t\left(J_l s^2 + K_s\right)}{J_m J_l s^3 + K_p K_t J_l s^2 + \left(J_m + J_l\right)K_s s + K_p K_t K_s} \quad (8)$$

The characteristic equation of (8) can be given as

$$s^3 + \frac{K_t K_p}{J_m}s^2 + \omega_{\mathrm{NTF}}^2 s + \frac{K_t K_p}{J_m}\omega_{\mathrm{ARF}}^2 = \left(s^2 + 2\xi_x\omega_x s + \omega_x^2\right)\left(s + K_x\right) = 0 \quad (9)$$

in which ζ_x and ω_x represent the damping and frequency coefficients of oscillating element respectively and the K_x is a coefficient that depends on the parameters of the system.

According to (3), the phase lag of the system in classical model is less than $\pi/4$. Thus, the drive system is bound to be stable if it is a minimum phase system. Based on (9), when $\zeta_x>0$ and $K_x>0$, the frequency of damped oscillation ω_e after speed loop returning to work can be given as

$$\omega_e = \omega_x\sqrt{1-\xi_x} \quad (10)$$

In summary, the mechanical resonance analyzed in classical model can be shown in Fig. 5. Because the oscillation in steady state decays gradually, the steady state oscillation is relatively small. Hence, the speed signal is given in the form of error in Fig.5. In transient state, speed error is the difference between the ramp component in (7) and speed feedback.

Besides the phenomena in Fig. 5, there is another type of mechanical resonance in modern digital drive system, which can be shown in Fig. 6. In the process of speed regulation, when speed reference is a step signal, speed loop saturates rapidly and current loop is able to track the constant reference from speed loop quickly in transient state. Thus, the influence of the digital control and current loop delay can both be ignored. The conventional model can still apply in transient state of Fig. 6. However, in steady state, the resonance in high gain system is a severe self-sustained oscillation with frequency is ω_{OSC} and sometimes ω_{OSC} is larger than ω_{NTF}. This phenomenon is different from the analysis of the conventional model. Hence, a more comprehensive model is needed.

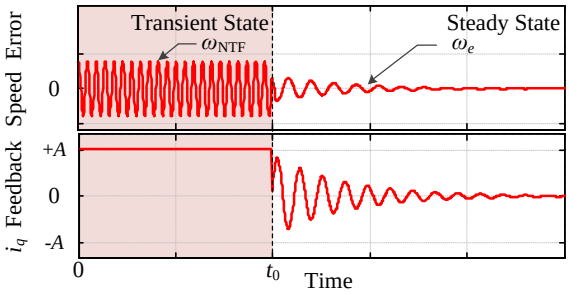

Fig. 5. Resonance in conventional mechanical model.

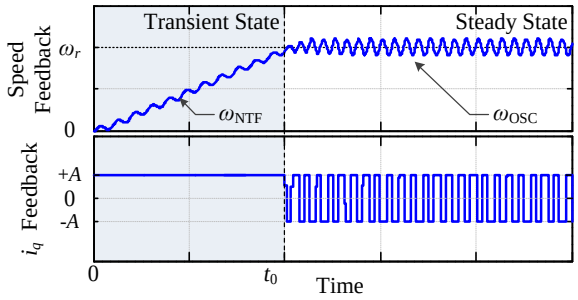

Fig. 6. Resonance in real digital servo system with elastic coupling. (The main control structure and most of the parameters are in consistent with those in Fig. 5, except the speed controller is discrete controller with sampling period T_{ASR}=1e-4s and the current loop is equivalent to $K_t e^{-\tau s}$ with τ=4e-4s instead of K_t. More introductions of this model can be found in Section III.)

III. Proposed Improved Mechanical Resonance Model in Elastic Coupling Digital Drive System

In mechanical resonance model for digital drive system, more factors need to be taken into account. In order to refine the conventional model, this part is focused on the modeling of three key factors including equivalence of current loop, impact of digital control and saturation nonlinearity of speed controller's output.

A. Equivalence of Current Loop

In traditional model, the current loop is usually regarded as torque coefficient K_t or first-order low pass filter because of its higher bandwidth than that of speed loop. However, due to the maximum phase lag of a first-order low pass filter is $\pi/2$ and the torque coefficient K_t does not provide any phase lag, the total phase lag is no more than π and the system is always stable under these two kinds of approximation methods. This conclusion conflicts with Fig. 6. In addition, the phase function of low pass filter includes inverse trigonometric function, which is not convenient for applied calculation.

Since the gain near ω_{NTF} is large, the amplitude attenuation from current loop can be ignored. Hence, this paper chooses delay model to simulate the current loop. In order to use delay model to reflect the bandwidth of current loop, the phase of the cutoff frequency ω_c is set as $-\pi/4$. The relationship between time constants, T_1 in delay model and T_c ($2\pi/\omega_c$) in current loop, can be given as

$$T_1 = \pi/\left(4\omega_c\right) = T_c/8 \quad (11)$$

The transfer function of the delay-model-based current loop can be given as

$$G_{\mathrm{ACR}}(s)=K_t e^{-sT_1}\Big|_{T_1=T_c/8}=K_t e^{-sT_c/8} \tag{12}$$

Taking (12) into consideration, the simplified open loop transfer function can be expressed as

$$G_{\mathrm{ACR}}(s)\cdot G_1(s)=\frac{J_l s^2+K_s}{\frac{J_m J_l}{(J_m+J_l)}s^2+K_s}\frac{1}{(J_m+J_l)s}\cdot K_t e^{-sT_c/8} \tag{13}$$

The phase of (13) can be expressed as

$$\angle G_{\mathrm{ACR}}(s)\cdot G_1(s)\big|_{s=\mathrm{j}\omega}=\begin{cases}-\dfrac{\omega T_c}{8}-\dfrac{\pi}{2},(\omega<\omega_{\mathrm{ARF}})\\ -\dfrac{\omega T_c}{8}+\dfrac{\pi}{2},(\omega_{\mathrm{ARF}}<\omega<\omega_{\mathrm{NTF}})\\ -\dfrac{\omega T_c}{8}-\dfrac{\pi}{2},(\omega>\omega_{\mathrm{NTF}})\end{cases} \tag{14}$$

B. Impact of Digital Control

Although digital control is flexible and widely used, it brings phase lag to system inevitably and affects the stability of the system. Hence, a ZOH with time constant T_{ASR} is added to the model to simulate the impact from digital control. T_{ASR} is also the sampling period of speed loop. The transfer function of ZOH $G_h(s)$ can be given as

$$G_h(s)=\left(1-e^{-T_{\mathrm{ASR}}s}\right)/s \tag{15}$$

Substituting $s=\mathrm{j}\omega$ into (15) yields

$$G_h(\mathrm{j}\omega)=T_{\mathrm{ASR}}\frac{\sin(\omega T_{\mathrm{ASR}}/2)}{\omega T_{\mathrm{ASR}}/2}e^{-\mathrm{j}\omega T_{\mathrm{ASR}}/2} \tag{16}$$

According to (16), the phase of $G_h(\mathrm{j}\omega)$ can be given as

$$\angle G_h(\mathrm{j}\omega)=e^{-\mathrm{j}\omega T_{\mathrm{ASR}}/2}=-\omega T_{\mathrm{ASR}}/2 \tag{17}$$

In order to unify those time constants, assuming T_{ACR} is the sampling period of current loop and p_1, p_2 are proportionality coefficients, which are related to the control strategy [26],[27]. In most cases, the description equations are as follows

$$\begin{cases}p_1=T_c/T_{\mathrm{ACR}}\geq 6\\ p_2=T_{\mathrm{ASR}}/T_{\mathrm{ACR}}\geq 1\end{cases} \tag{18}$$

Adding (15) and $G_{\mathrm{ASR}}(s)$ into (13), using (18) to unify those time constants as multiples of T_{ACR} and extracting the phase component of ZOH only. The open loop transfer function of digital control system $T(s)$ can be expressed as

$$T(s)=G_h(s)\cdot G_{\mathrm{ASR}}(s)\cdot G_{\mathrm{ACR}}(s)\cdot G_1(s)$$
$$=\frac{J_l s^2+K_s}{\frac{J_m J_l}{(J_m+J_l)}s^2+K_s}\frac{1}{(J_m+J_l)s}\cdot K_p K_t e^{-\left(\frac{p_1+4p_2}{8}\right)T_{\mathrm{ACR}}s} \tag{19}$$

The phase of (19) can be expressed as

$$\angle T(s)\big|_{s=\mathrm{j}\omega}=\theta_h+\theta_{\mathrm{ACR}}+\theta_1$$
$$=\begin{cases}-\left(\dfrac{p_1+4p_2}{8}\right)T_{\mathrm{ACR}}\omega-\dfrac{\pi}{2},(\omega<\omega_{\mathrm{ARF}})\\ -\left(\dfrac{p_1+4p_2}{8}\right)T_{\mathrm{ACR}}\omega+\dfrac{\pi}{2},(\omega_{\mathrm{ARF}}<\omega<\omega_{\mathrm{NTF}})\\ -\left(\dfrac{p_1+4p_2}{8}\right)T_{\mathrm{ACR}}\omega-\dfrac{\pi}{2},(\omega>\omega_{\mathrm{NTF}})\end{cases} \tag{20}$$

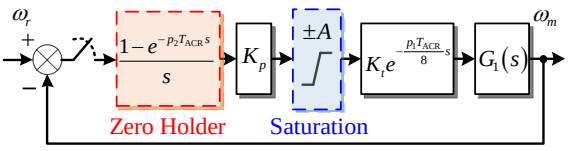

Fig. 7. Control diagram of two-mass discrete servo system with speed output saturation.

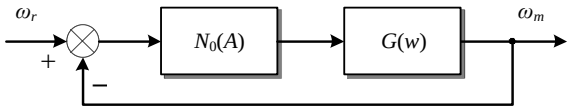

Fig. 8. Nonlinear control block diagram.

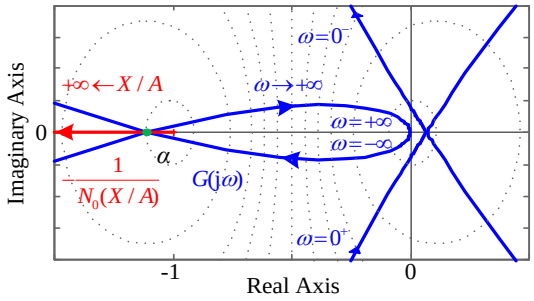

Fig. 9. Nyquist curve of system.

According to (20), there is enough phase lag in the modified transfer function $T(s)$ rather than the conventional model. It means that if the gain of system is large and the phase margin is negative, the system becomes unstable and the subsequent oscillation inferred from the above analysis is more realistic.

C. Saturation Nonlinearity of Speed Controller's Output

In linear control theory, the prerequisite for undamped self-sustaining oscillation is rigorous. Thus, damped or divergent oscillation is more common. However, there is an undamped self-sustaining oscillation in steady state of Fig. 6. In order to explain this phenomenon, the nonlinear analysis method is used. The describing function of saturation nonlinearity of speed controller's output (output limit is $\pm A$) can be given as

$$N_0\left(\frac{X}{A}\right)=\frac{2}{\pi}\left[\arcsin\frac{A}{X}+\frac{A}{X}\sqrt{1-\left(\frac{A}{X}\right)^2}\right] \tag{21}$$

The control diagram of improved mechanical resonance model can be shown in Fig. 7. In order to simplify the operation, this part reunifies those time constants as multiples of T_{ASR}. Next, assuming $\lambda=p_1/8p_2$ and substituting the whole ZOH into the system transfer function. The open loop transfer function of system in the z-domain $G(z)$ can be expressed as [23],[24]

$$G(z)=Z\left\{K_p K_t e^{-s\lambda T_{\mathrm{ASR}}}G_h(s)G_1(s)\right\}=K_p K_t\frac{z-1}{z^{\ell}+1}Z\left\{\frac{G_1(s)}{s}e^{smT_{\mathrm{ASR}}}\right\} \tag{22}$$

in which ℓ is an integer, $0\leq m<1$, and $\ell=\lambda+m$. According to the method of residues, (22) can be rewritten as

$$Z\left\{\frac{G_1(s)}{s}e^{smT_{\mathrm{ASR}}}\right\}=\sum_{i=1}^{n}\mathrm{Res}\left[\frac{zG_1(s)e^{smT_{\mathrm{ASR}}}}{s\left(z-e^{sT_{\mathrm{ASR}}}\right)}\right]_{s=p_i} \tag{23}$$

Substituting (3) into (23) yields

$$G(z)=K_pK_t\frac{z-1}{z^{\ell}}\Big[\frac{T_{\mathrm{ASR}}}{J_m+J_l}\frac{mz+1-m}{(z-1)^2}+\frac{J_l}{J_m(J_m+J_l)\omega_{\mathrm{NTF}}}\frac{z\sin m\omega_{\mathrm{NTF}}T_{\mathrm{ASR}}+\sin(1-m)\omega_{\mathrm{NTF}}T_{\mathrm{ASR}}}{z^2-2z\cos\omega_{\mathrm{NTF}}T_{\mathrm{ASR}}+1}\Big] \tag{24}$$

The w-transform $z=(w+1)/(w-1)$ is used to transform (24) from z-transform to w-transform. By separating the linear part and nonlinear part, Fig. 7 can be reconfigured to Fig. 8. The negative inverse describing function curve $-1/N_0(X/A)$ and the linear transfer function curve $G(w)$ are both plotted in Fig. 9 (the crossover point is α). According to the describing function method [28], if the amplitude of oscillation becomes larger, the action point departs from the surroundings of $G(w)$ and the system restores stability. Finally, the action point returns to α again. In contrast, if the amplitude of oscillation becomes smaller, the action point moves to the right of the α. Right part of $-1/N_0(X/A)$ is surrounded by $G(w)$, which means the system becomes unstable and the oscillation amplitude becomes larger. Then, the action point moves back to α as well. Hence, the crossover point α corresponds with undamped self-sustaining oscillation and the frequency of α is the oscillation frequency ω_{OSC}. Because $-1/N_0(X/A)$ must be a negative real number less than -1, if α exists, it must locate on the negative real axis. Thus, there is a phase relationship of ω_{OSC} as follows

$$\angle G\left(\mathrm{j}\omega_{\mathrm{OSC}}\right)=\angle -1/N_0\left(X/A\right)=-\pi \tag{25}$$

In order to simplify the operation, (20) is used to replace $G(w)$ in (25). Then, the expression of ω_{OSC} can be given as (because for the sake of work efficiency the phase lag of real system cannot be too large, the possibility of $-\pi$ crossover point takes place near or before ω_{ARF} is small, so it is ignored)

$$\omega_{\mathrm{OSC}}=\begin{cases}\omega_{\mathrm{NTF}} & ,\left\{\angle T\left(\mathrm{j}\omega_{\mathrm{NTF}_-}\right)>-\pi\cap\angle T\left(\mathrm{j}\omega_{\mathrm{NTF}_+}\right)<-\pi\right\}\\ \dfrac{4\pi}{\left(p_1+4p_2\right)T_{\mathrm{ACR}}} & ,\left\{\angle T\left(\mathrm{j}\omega_{\mathrm{NTF}_+}\right)>-\pi\right\}\end{cases} \tag{26}$$

In this paper, the frequency deviation means $\omega_{\mathrm{OSC}}>\omega_{\mathrm{NTF}}$. According to (20) and (26), the calculation formula of shifted frequency ω_{OSC} of the system and its deviation criterion can be given as (transforming the frequency unit to Hertz ($\omega=2\pi f$))

$$f_{\mathrm{OSC}}=2/\left(T_c+4T_{\mathrm{ASR}}\right)\ \ ,\left\{T_c+4T_{\mathrm{ASR}}<2/f_{\mathrm{NTF}}\right\} \tag{27}$$

According to (27), the impact of T_c and T_{ASR} on f_{OSC} can be shown as Fig. 10. With the decrease of the delay from current and speed loop, f_{OSC} gradually increases. In the previous industrial drive system, T_c and T_{ASR} is relatively large. Hence, almost all f_{OSC} in system are equal to f_{NTF}. However, high performance and bandwidth become the characteristics of modern digital control systems. The decrease of the system delay means ω_{OSC} would be more likely to deviate from ω_{NTF}.

To sum up, the decrease of T_c and T_{ASR} are key factors for oscillation frequency deviation; the saturation nonlinearity coming from the limitation of speed loop output is the cause of the undamped self-sustaining oscillation of systems in steady state when the phase margin of the system is negative. The saturation avoids the occurrence of severer diverging oscillation and protects the systems (tuning A can constrain the maximum oscillation amplitude). Based on the improved model, the expression of ω_{OSC} and a deviation criterion of oscillation frequency (27) are concluded. Because (27) is concise and intuitive, it can be applied in reality to identify whether the resonance deviation happens or not.

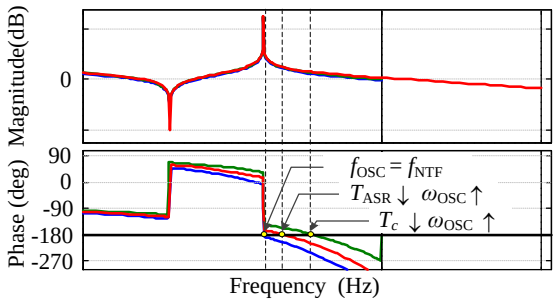

Fig. 10. Deviation of oscillation frequency

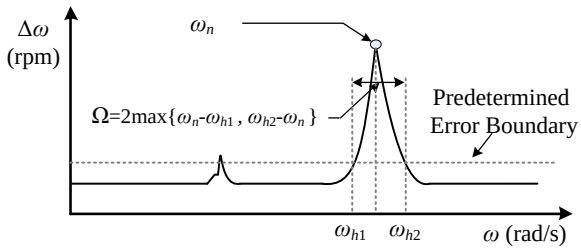

Fig. 11. Parameters determination of classical notch filter.

IV. Proposed Robust Notch Filter Strategy

A. Traditional On-Line Adaptive Notch Filter Theory

The transfer function of classical notch filter can be given as

$$G_n\left(s\right)=\frac{s^2+\omega_n^2}{s^2+bs+\omega_n^2} \tag{28}$$

where ω_n is the notch frequency and b is -3dB rejection bandwidth factor. The phase of (28) around ω_n can be given as

$$\begin{cases}\angle G_n\left(\mathrm{j}\omega_{n-}\right)=\arctan\left[b\omega_{n-}/\left(\omega_{n-}^2-\omega_n^2\right)\right]=-\pi/2\\ \angle G_n\left(\mathrm{j}\omega_{n+}\right)=\arctan\left[b\omega_{n+}/\left(\omega_{n+}^2-\omega_n^2\right)\right]=+\pi/2\end{cases} \tag{29}$$

Assuming $k=2/T_{\mathrm{ASR}}$, Ω is the rejection bandwidth and the magnitude of notch filter at $\omega_n\pm\Omega/2$ is $-x$. Applying Tustin transformation to discretize the notch filter (28) and DFIIt structure [8],[23] to modify the notch factor yields

$$G_n\left(z\right)=\frac{1}{2}\cdot\frac{\left(1+a_2\right)-2a_1z^{-1}+\left(1+a_2\right)z^{-2}}{1-a_1z^{-1}+a_2z^{-2}} \tag{30}$$

in which a_1 and a_2 can be express as

$$\begin{cases}a_1=\dfrac{2\cos\omega_nT_{\mathrm{ASR}}}{1+\sqrt{10^{x/10}-1}\tan\left(\Omega T_{\mathrm{ASR}}/2\right)}\\ a_2=\dfrac{1-\sqrt{10^{x/10}-1}\tan\left(\Omega T_{\mathrm{ASR}}/2\right)}{1+\sqrt{10^{x/10}-1}\tan\left(\Omega T_{\mathrm{ASR}}/2\right)}\end{cases} \tag{31}$$

One of the conventional OANF parameter tuning methods can be shown in Fig. 11. A predetermined error boundary is set to get the rejection bandwidth Ω, and the on-line FFT result of speed feedback error signal is used to find the notch frequency ω_n in this method [6]. After parameter determination, according to (24) and (30), the open loop transfer function of the system with notch filter $G^*(z)$ can be given as

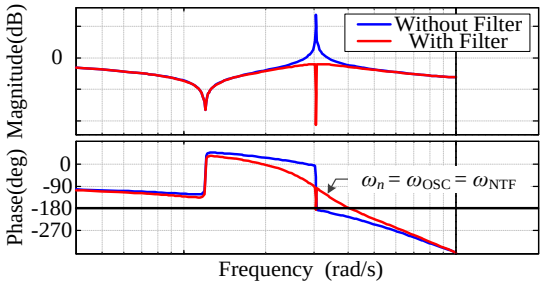

Fig. 12. Bode diagram of classical notch filter effect when $\omega_{OSC}=\omega_{NTF}$.

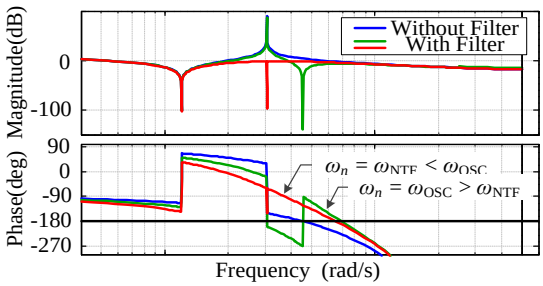

Fig. 13. Mechanical resonance suppression effect of different notch frequencies when $\omega_{OSC}>\omega_{NTF}$.

$$G^*(z) = G(z)G_n(z) \tag{32}$$

By substituting $z=(w+1)/(w-1)$ into (32), when $\omega_{OSC}=\omega_{NTF}$, the bode diagram of $G^*(w)$ can be shown in Fig. 12. According to Fig. 12 and (29), OANF can not only decrease the gain around ω_{NTF} but also reduce the phase lag after ω_{NTF} at the cost of increase the phase lag before ω_{NTF}. The improvement from both magnitude and phase characteristics make system restore stability effectively. However, in Fig. 13, different with Fig. 12, the criterion in (27) is valid and ω_{OSC} is larger than ω_{NTF}. The phase delay coming from OANF causes the new ω_{OSC} to move closer to ω_{NTF} and even result in a server oscillation. Thus, OANF is not suitable in the condition of $\omega_{OSC}>\omega_{NTF}$.

B. Process of Robust On-line Adaptive Notch Filter

Also based on Fig. 13, if ω_{NTF} is set as ω_n, the notch filter can still make up for the phase lag around the ω_{OSC} to guarantee the stability of system. Hence, no matter whether the criterion in (27) is valid or not, $\omega_n=\omega_{NTF}$ is an effective choice. Considering the time of transient-state oscillation with frequency is ω_{NTF} is relatively short and the FFT analysis is not reliable, thus, the steady state on-line identification of ω_{NTF} is the focus of proposed ROANF strategy.

According to (27) and Fig. 10, T_{ASR} and T_c are influencing factors for ω_{OSC} in drive system. An appropriate increase for T_{ASR} or T_c can make criterion in (27) invalid again and ω_{OSC} return to ω_{NTF}. Because the parameters of the current loop controller need to be conservative enough to ensure the security of system, the adjustment of T_{ASR} is finally adapted in ROANF to extract ω_{NTF} of system. In addition, because larger T_{ASR} means larger oscillation amplitude, the output limit of speed loop A is reduced moderately before ROANF parameters identification is finished. Overall, the control diagram and schematic diagram (T_{ASR0} is the initial sampling period of speed loop and it is assumed to be no longer than 2ms) of ROANF can be shown as Fig. 14 and Fig. 15 respectively, and the detailed process of ROANF is listed as follows

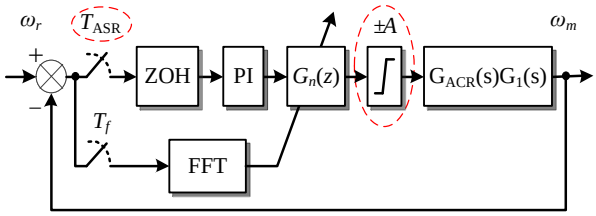

Fig. 14. Diagram of ROANF.

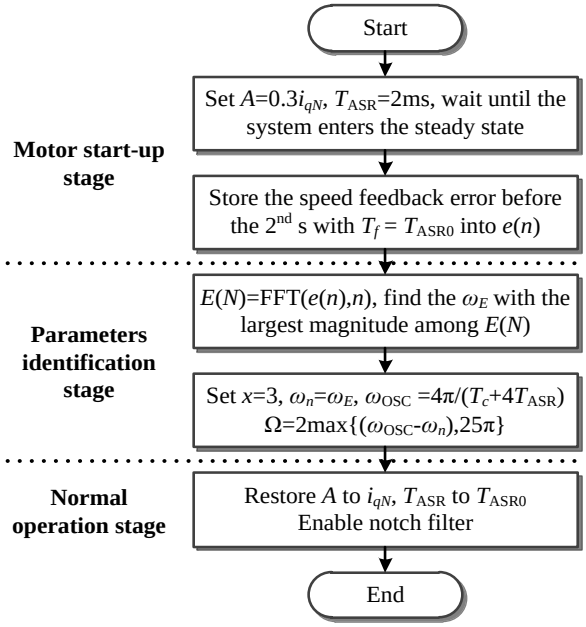

Fig. 15. Schematic diagram of ROANF.

1) Motor start-up stage: Because common audible resonance frequency in the servo system ranges from 100 to 300Hz [1], T_{ASR} can be increased to around 2ms. To simplify the operation, the sampling period of FFT T_f is a constant (equal to T_{ASR0}). In addition, output limit of the speed controller A can be decreased by 50~80 percent. Then, let the system track the speed reference normally and the whole stage takes around 2 seconds to store enough speed feedback data for the FFT analysis.
2) Parameters identification stage: In this stage, FFT is used to extract ω_{NTF} of system from the data acquired in stage I. In order to suppress amplitude gain around ω_{OSC}, notch filter rejection bandwidth Ω can be calculated as

$$\Omega = 2\max\left\{\left(\omega_{OSC} - \omega_{NTF}\right), 25\pi\right\} \tag{33}$$

where ω_{OSC} can be computed from (27). Considering $\omega_{OSC}=\omega_{NTF}$ in some cases, 50π is set as the lower bound of Ω. Notch depth coefficient x is depended on the oscillation amplitude. Normal range of x is 3~10dB.
3) Normal operation stage: Enable the notch filter and recover the T_{ASR} and A of controller.

V. Experimental Results

The experiment setup is shown in Fig. 16, consisting of a Zynq-based driver and a DSP-based driver, two SPMSMs and two elastic couplings. Two SPMSMs are both equipped with 2500 impulses/revolution incremental optical encoders. The

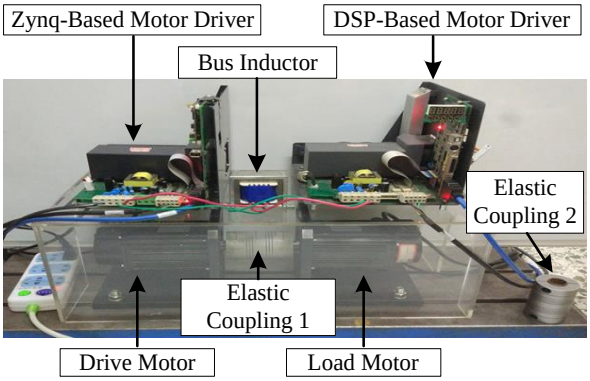

Fig. 16. Experiment setup.

TABLE I
MAIN PARAMETERS OF PMSM DRIVE SYSTEM

Parameter	nominal value
Motor Power P_N	750 W
Nominal Torque T_{eN}	2.39 N·m
Nominal Speed ω_N	3000 r/min
Nominal Current i_{qN}	3 A
Inertia of drive motor J_m	1.82e-4 kg·m^2
Inertia of load motor J_l	1.82e-4 kg·m^2
Stiffness of elastic coupling 1 K_{s1}	91 N·m/rad
Stiffness of elastic coupling 2 K_{s2}	149 N·m/rad

period of current control loop is 0.1ms. The focus of the ROANF is to identify the ω_{NTF} on-line under the assumption that the parameter of the elastic coupling is unknown or inaccurate. Thus, the tuning of the speed PI controller in this paper is based on the classical strategy of solid coupling drive system. In brief, the proportional constant K_p can be roughly considered to be proportional to the bandwidth of speed loop. In the experiment, K_p(=40) and K_i(=2.5) of speed loop controller are set as high-gain constants before discretization in the experiments. The specifications are presented in Table I. The unit of oscillation frequency in this part is chosen as Herz. ROANF is built in the Zynq-based driver, and the DSP-based driver is used to provide a nominal torque as disturbance. About the Zynq-based motor driver, the control chip is Xilinx Zynq series SoC, which integrates ARM (two Cortex-A9s but only one is used) and FPGA into one chip. The communication between ARM and FPGA is realized by AXI bus inside SoC. In addition, the RAM of Zynq is extended to 1GB by adding external memory chip to record experiment data. FPGA is responsible for the current loop control (a classical PI controller is used) and the FFT analysis. The speed loop control and ROANF is finished in ARM. When each time current loop control is finished in FPGA, an external interrupt is sent to ARM and a register is used to record the times of interrupts to judge the frequency (corresponding to sampling period) of speed loop control. Hence, T_{ASR} can be adjusted easily. In addition, a series of predetermined PI parameters of current loop controller are adapted to change T_c of the system. In order to describe the influence of delays in current control loop directly and the selection criteria for cutoff time constant T_c. One kind of sweep signals—Chirp Signal (the frequency of which increases with time) is used as i_{qref}. Then, FFT analyzes

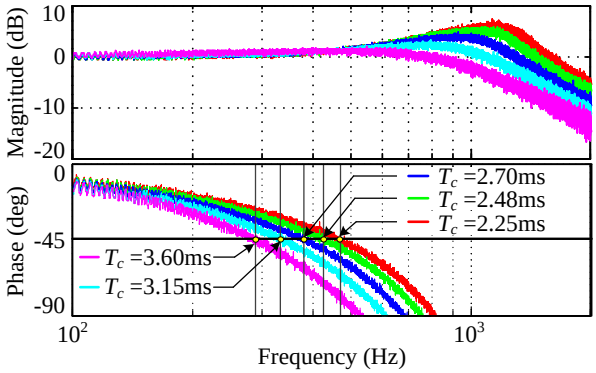

Fig. 17. Analysis results of current loop with different parameters.

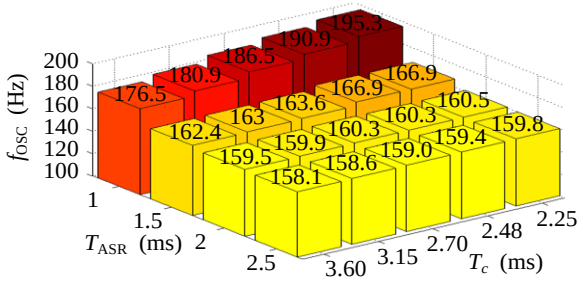

Fig. 18. Oscillation frequency of systems with different T_{ASR} and T_c.

the relationship between i_{qref} and i_q feedback to identify the frequency domain characteristics of the current loop and get the value of T_c. The analysis results of current loop with different parameters are shown in Fig. 17.

Apart from the modification of current limitation and speed loop sampling period, only the parameters of speed controller's output filter are changeable. Especially, in order to reflect the importance of the choice for notch frequency ω_n and to enhance the contrast effects with the performance of OANF, both Ω and x of OANF and ROANF are set as 100π and 3 instead of self-tuning. Thus, only ω_n is the changeable in OANF and ROANF settings for the follow-up experiments.

A. Oscillation Frequency Deviation Phenomenon

At first, off-line two-mass mechanical systems identification [29],[30] is used to determine the standard value f_{NTF} of the systems that are coupled by elastic coupling 1 (f_{NTF} =159Hz) and elastic coupling 2 (f_{NTF} =203Hz). Considering the results of these two kinds of couplings are similar, only the data of coupling 1 is given out. In order to verify the validity of the proposed model, oscillation frequencies f_{OSC} of the platform with different T_{ASR} (from 1ms to 2.5ms) and T_c (from 2.25ms to 3.60ms) are recorded in Fig. 18.

According to Fig. 18, when $T_{\mathrm{ASR}}\geq$2ms, f_{OSC} is close to f_{NTF} (159Hz). However, when $T_{\mathrm{ASR}}<$2ms, f_{OSC} shifts from f_{NTF} to a higher frequency. f_{OSC} tends to increase with the decrease of T_{ASR} and T_c. Submitting the groups of data $T_{\mathrm{ASR}}<$2ms from Fig. 18 into (27) indicates error remains several tens of Hertz from expected f_{OSC}. Thus, assuming $G_m(s)=e^{-sTm}$ as the modification factor to reflect the delay coming from damping, signal filtering and transmission. Combining $G_m(s)$ with (27), the fixed expression and criterion can be given as

$$f_{\mathrm{OSC}} = 2/\left(T_c + 4T_{\mathrm{ASR}} + 8T_m\right),\left\{T_c + 4T_{\mathrm{ASR}} + 8T_m < 2/f_{\mathrm{NTF}}\right\} \quad (34)$$

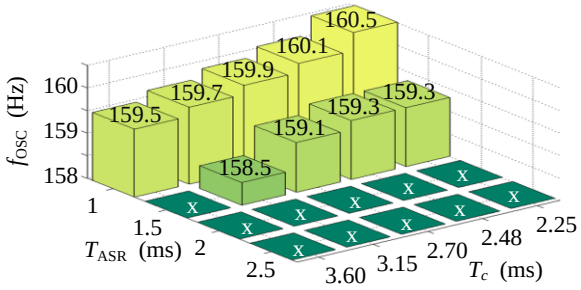

(a) New f_{OSC} after OANF is enabled (the white 'x' means system restores stable)

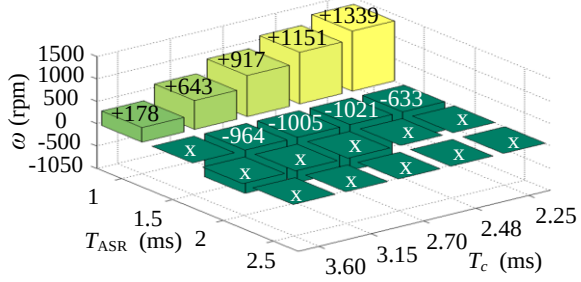

(b) Oscillation amplitude variation of the systems after OANF is enabled (the white 'x' means system restores stable)

Fig. 19. Effect of OANF.

in which T_m can be calculated by taking data from Fig. 18 to (34) and calculating the arithmetic mean.

By setting T_m as 0.4531ms, estimation error has been narrowed down to several Hertz, which is within acceptable range. In addition, the parameter conservation from (27) does not cause the failure of ROANF because the determined Ω is larger than the required minimum rejection bandwidth.

New oscillation frequency f_{OSC} and oscillation amplitude variation of the system after OANF is enabled are shown in Fig. 19 (a) and Fig. 19 (b) respectively. In case of $f_{OSC}\approx f_{NTF}$, OANF can suppress resonance successfully. However, when $f_{OSC}>f_{NTF}$, OANF causes a lower frequency oscillation with an amplitude even hundreds rpm larger (in the case of T_{ASR}=1ms), which is consistent with previous derivations.

B. Resonance Damping Test without Load Torque

For verifying the effectiveness of ROANF, two sets of comparative experiments in the case of $f_{OSC}>f_{NTF}$ and $f_{OSC}=f_{NTF}$ are carried out and the results are shown in Fig. 20. The Fig. 20 (a) and (c) are the speed and current responses with OANF and ROANF. In addition, the Fig. 20 (b) and (d) are FFT results of speed error signal during 5~6s (before notch filter is enabled) and 7~8s (after notch filter is enabled) respectively for Fig. 20 (a) and (c). *A* of OANF and ROANF is both set as 3A. However, T_{ASR} and *A* of ROANF are adjusted to 2ms and 0.9A at motor start-up stage. In the experiment, there is an oscillation frequency identifying process about 2s in OANF and ROANF.

In Fig. 20 (a) and (b), when $f_{OSC}>f_{NTF}$, because oscillation frequency has deviated, the enable of OANF lowers the frequency (159.5Hz) and makes its amplitude larger (+178rpm). In contrast, T_{ASR} adjustment of ROANF make f_{OSC} return to f_{NTF} effectively. Then, the correct notch frequency identification achieved a good resonance damping performance.

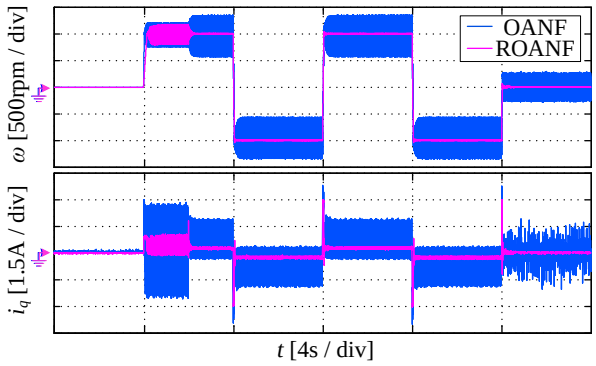

(a) The case of $f_{OSC}>f_{NTF}$, T_{ASR}=1ms, T_c=3.6ms

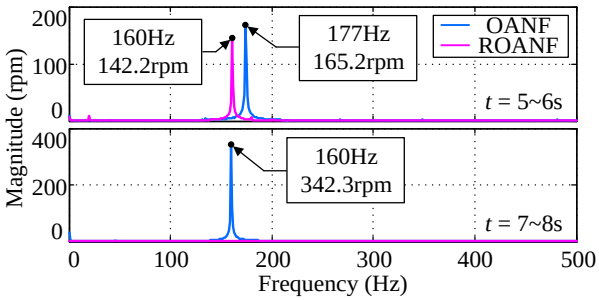

(b) FFT results of speed error signal during 5~6s and 7~8s, in the case of $f_{OSC}>f_{NTF}$, T_{ASR}=1ms, T_c=3.6ms

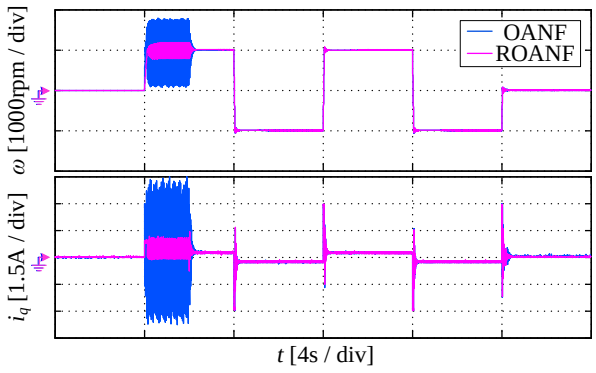

(c) The case of $f_{OSC}=f_{NTF}$, T_{ASR}=2ms, T_c=3.6ms

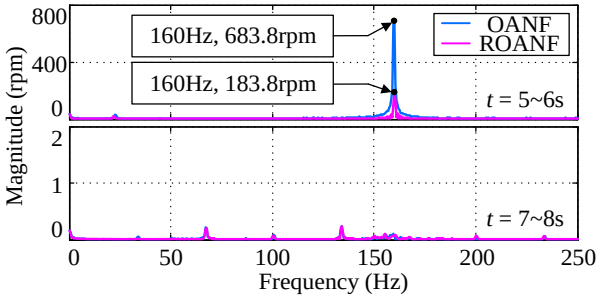

(d) FFT results of speed error signal during 5~6s and 7~8s, in the case of $f_{OSC}=f_{NTF}$, T_{ASR}=2ms, T_c=3.6ms

Fig. 20. Speed and current responses with OANF and ROANF.

Besides, in Fig. 20 (c) and (d), when $f_{OSC}=f_{NTF}$, T_{ASR} is 2ms at first and no more adjustment of T_{ASR} is needed for ROANF. Although both OANF and ROANF make system stable, the adjustment of ROANF's speed output limit decreases the oscillation amplitude and ensures the safety of the equipment.

This article has been accepted for publication in a future issue of this journal, but has not been fully edited. Content may change prior to final publication. Citation information: DOI 10.1109/TIE.2018.2825300, IEEE Transactions on Industrial Electronics

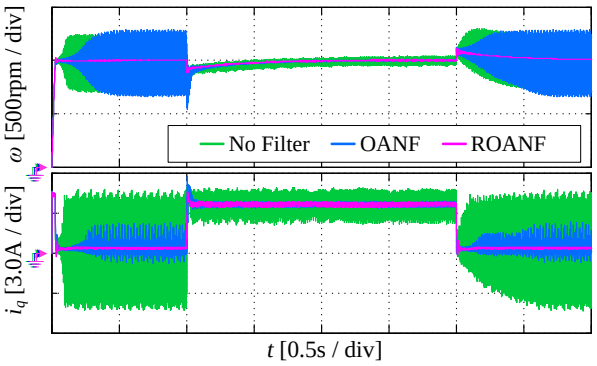

Fig. 21. Experimental results under nominal torque load with different control strategies.

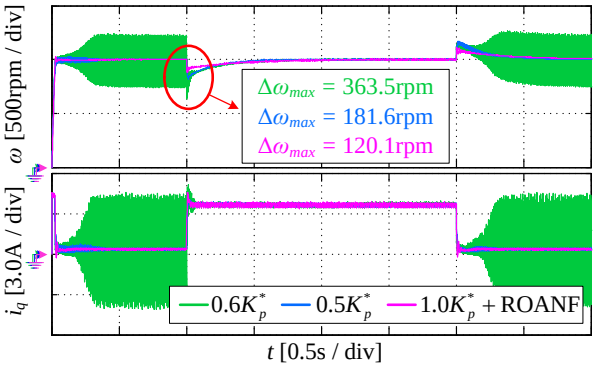

Fig. 22. Experimental results under nominal torque load with different speed controller parameters.

C. Resonance Damping Test with Different Control Strategies and Parameters under Nominal Torque Load

To test the system's ability of resisting disturbances under nominal torque load, the results with different control strategies and different speed controller parameters are shown in Fig. 21 and Fig. 22 respectively.

In Fig. 21, ω_n identification of OANF and ROANF are assumed to be finished. In addition, considering the load torque is a nominal torque 2.39N m (corresponds to nominal current 3A of *q*-axis) and taking those friction and damping torque into account, the output limitation of speed controller *A* is expanded to 4.5A. A nominal load is injected at the 1st s and removed at the 3rd s. The results prove the effectiveness of the ROANF under switching of the load during steady state.

In Fig. 22(K_p^* =40), there are three groups of loading experiments including K_p=0.5K_p^* , K_p=0.6K_p^* and K_p=1.0K_p^* (when K_p=1.0K_p^* ROANF is added into control loop. In other cases, only a PI controller is used). Based on the experiment results, the system becomes unstable when the gain of controller is increased to 0.6K_p^* . However, after ROANF is added to system, the system is still stable when the gain of controller is even increased to 1.0K_p^* and with the minimum speed drop (120.1rpm). In addition, it is worth mentioning that when a suitable smaller K_p (<0.5K_p^*) is chosen, the jitter at the time of system entering steady state can also be damped slightly. However, a smaller K_p also means a worse anti disturbance ability (according to Fig. 22). Hence, dislike ROANF, although decreasing the gain of controller is a simpler solution, it cannot guarantee both disturbance rejection and stability.

In conclusion, experiment results verify the effectiveness of oscillation frequency deviation criterion and the robustness and disturbances rejection ability of ROANF.

VI. Conclusion

This paper has classified several kinds of mechanical resonance in elastic coupling drive system. In order to identify the severe self-sustained oscillation in steady state of high-performance digital drive system, an improved digital drive mechanical resonance model has been built up by taking delay of current loop, influence of digital control and saturation nonlinearity in speed loop into consideration. Based on this model, the phenomenon that system's oscillation frequency deviated from the natural torsional frequency is discussed and an oscillation frequency deviation criterion is obtained. Finally, a robust on-line adaptive notch filter is proposed. Appropriate adjustments of sampling period and output limit of speed loop are used to identify the correct notch frequency and achieve robust and effective resonance damping in different systems. Both the oscillation frequency deviation analysis and the performance of robust on-line adaptive notch filter are verified on an elastic coupling PMSM platform. The future work will focus on analyzing the influence of damping in mechanical resonance frequency and testing other types of suppression methods in systems with oscillation frequency deviation.

References

[1] S. N. Vukosavic, and M. R. Stojic, "Suppression of torsional oscillations in a high-performance speed servo drive," *IEEE Trans. Ind. Electron.*, vol. 45, no. 1, pp. 108-117, Feb. 1998.

[2] C. Ma, J. Cao, and Y. Qiao, "Polynomial-Method-Based Design of Low-Order Controllers for Two-Mass Systems," *IEEE Trans. Ind. Electron.*, vol. 60, no. 3, pp. 969-978, Mar. 2013.

[3] T. M. O'Sullivan, C. M. Bingham, and N. Schofield, "High-Performance Control of Dual-Inertia Servo-Drive Systems Using Low-Cost Integrated SAW Torque Transducers," *IEEE Trans. Ind. Electron.*, vol. 53, no. 4, pp. 1226-1237, Jun. 2006.

[4] S. Yang, and S. Wang, "The Detection of Resonance Frequency in Motion Control Systems," *IEEE Trans. Ind. Appl.*, vol. 50, no. 5, pp. 3423-3427, Sept/Oct. 2014.

[5] J. Kang, S. Chen, and X. Di, "Online detection and suppression of mechanical resonance for servo system," in *Proc. ICICIP*, 2012, pp. 16-21.

[6] D. -H. Lee, J. H. Lee, and J. -W. Ahn, "Mechanical vibration reduction control of two-mass permanent magnet synchronous motor using adaptive notch filter with fast Fourier transform analysis," *IET Electric Power Appl.*, vol. 6, no. 7, pp. 455-461, Aug. 2012.

[7] W. Wang, J. Xu, and A. Shen, "Detection and reduction of middle frequency resonance for industrial servo," in *Proc. ICIST*, 2012, pp. 153-160.

[8] K. Hirano, S. Nishimura, and S. K. Mitra, "Design of Digital Notch Filters," *IEEE Trans. Circuits Syst.*, vol. 21, no. 4, pp. 540-546, Jul. 1974.

[9] C. Wang, M. Zheng, Z. Wang, and M. Tomizuka, "Robust Two-Degree-of-Freedom Iterative Learning Control for Flexibility Compensation of Industrial Robot Manipulators," in *Proc. ICRA*, 2016, pp. 2381-2386.

[10] S. E. Saarakkala, and M. Hinkkanen, "State-Space Speed Control of Two-Mass Mechanical Systems: Analytical Tuning and Experimental Evaluation," *IEEE Trans. Ind. Appl.*, vol. 50, no. 5, pp. 3428-3437, Sept/Oct. 2014.

[11] K. Szabat, and T. Orlowska-Kowalska, "Vibration Suppression in a Two-Mass Drive System Using PI Speed Controller and Additional Feedbacks—Comparative Study," *IEEE Trans. Ind. Electron.*, vol. 54, no. 2, pp. 1193-1206, Apr. 2008.

[12] K. Erenturk, "Fractional-Order *hboxPI*^{lambda}*hboxD*^{mu} and Active Disturbance Rejection Control of Nonlinear Two-Mass Drive System," *IEEE Trans. Ind. Electron.*, vol. 60, no. 9, pp. 3806-3813, Sept. 2013.

[13] K. Szabat, and T. Orlowska-Kowalska, "Application of the Kalman Filters to the High-Performance Drive System With Elastic Coupling," *IEEE Trans. Ind. Electron.*, vol. 59, no. 11, pp. 4226-4235, Nov. 2012.
[14] S. Thomsen, N. Hoffmann, and F. W. Fuchs, "PI Control, PI-Based State Space Control, and Model-Based Predictive Control for Drive Systems With Elastically Coupled Loads—A Comparative Study," *IEEE Trans. Ind. Electron.*, vol. 58, no. 8, pp. 3647-3657, Aug. 2011.
[15] E. Fuentes, D. Kalise, and R. M. Kennel, "Smoothened Quasi-Time-Optimal Control for the Torsional Torque in a Two-Mass System," *IEEE Trans. Ind. Electron.*, vol. 63, no. 6, pp. 3954-3963, Jun. 2016.
[16] E. Fuentes, and R. M. Kennel, "A finite-set model predictive position controller for the permanent magnet synchronous motor," in *Proc. SLED/PRECEDE*, 2013, pp. 1-7.
[17] P. J. Serkies, and K. Szabat, "Application of the MPC to the Position Control of the Two-Mass Drive System," *IEEE Trans. Ind. Electron.*, vol. 60, no. 9, pp. 3679-3688, Sept. 2013.
[18] E. J. Fuentes, C. A. Silva, and J. I. Yuz, "Predictive Speed Control of a Two-Mass System Driven by a Permanent Magnet Synchronous Motor," *IEEE Trans. Ind. Electron.*, vol. 59, no. 7, pp. 2840-2848, Jul. 2012.
[19] K. Szabat, T. Orlowska-Kowalska, and M. Dybkowski, "Indirect Adaptive Control of Induction Motor Drive System With an Elastic Coupling," *IEEE Trans. on Ind. Electron.*, vol. 56, no. 10, pp. 4038-4042, Oct. 2009.
[20] K. Szabat, T. Tran-Van, and M. Kamiński, "A Modified Fuzzy Luenberger Observer for a Two-Mass Drive System," *IEEE Trans. Ind. Informat.*, vol. 11, no. 2, pp. 531-539, Apr. 2015.
[21] T. Orlowska-Kowalska, M. Dybkowski and K. Szabat, "Adaptive Sliding-Mode Neuro-Fuzzy Control of the Two-Mass Induction Motor Drive Without Mechanical Sensors," *IEEE Trans. on Ind. Electron.*, vol. 57, no. 2, pp. 553-564, Feb. 2010.
[22] K. Peter, I. Scholing, and B. Orlik, "Robust output-feedback H_∞ control with a nonlinear observer for a two-mass system," *IEEE Trans. Ind. Appl.*, vol. 39, no. 3, pp. 637-644, May/Jun. 2003.
[23] W. Yao, Y. Yang, X. Zhang, F. Blaabjerg, and P. C. Loh, "Design and Analysis of Robust Active Damping for LCL Filters Using Digital Notch Filters," *IEEE Trans. Power Electron.*, vol. 32, no. 3, pp. 2360-2375, Mar. 2016.
[24] J. Wang, J. Yan, L. Jiang, and J. Zou, "Delay-Dependent Stability of Single-Loop Controlled Grid-Connected Inverters with LCL Filters," *IEEE Trans. Power Electron.*, vol. 31 no. 1, pp. 743-757, Jan. 2016.
[25] R. Peña-Alzola, M. Liserre, F. Blaabjerg, M. Ordonez, and Y. Yang, "LCL-Filter Design for Robust Active Damping in Grid-Connected Converters," *IEEE Trans. Ind. Informat.*, vol. 10, no. 4, pp. 2192-2203, Nov. 2014.
[26] E. Jung, H. Lee, and S. Sul, "FPGA-based motion controller with a high bandwidth current regulator," in *Proc. PESC*, 2008, pp. 3043-3047.
[27] X. Zhang, J. Chen, Y. Ma, Y. Wang, and D. Xu, "Bandwidth Expansion Method for Circulating Current Control in Parallel Three-phase PWM Converter Connection System," *IEEE Trans. Power Electron.*, vol. 29 no. 12, pp. 6847-6856, Dec. 2014.
[28] M. Yang, C. Wang, W. Zheng, K. Hu and D. Xu, "Analysis and Suppression of Limit Cycle Oscillation for Transmission System with Backlash Nonlinearity," *IEEE Trans. on Ind. Electron.*, vol. 64, no. 12, pp. 9261-9270, Dec. 2017.
[29] Z. Henning, and M. Pacas, "Encoderless Identification of Two-Mass-Systems Utilizing an Extended Speed Adaptive Observer Structure," *IEEE Trans. Ind. Electron.*, vol. 64, no. 1, pp. 595-604, Jan. 2016.
[30] S. E. Saarakkala, and M. Hinkkanen, "Identification of Two-Mass Mechanical Systems Using Torque Excitation: Design and Experimental Evaluation," *IEEE Trans. Ind. Appl.*, vol. 51, no. 5, pp. 1922-1930, Sept/Oct. 2015.

Yangyang Chen received the B.S. degree in electrical engineering in 2016 from Harbin Institute of Technology, Harbin, China, where he is currently working toward the Ph.D. degree in power electronics and electrical drives in the School of Electrical Engineering and Automation.

His current research interest focuses on multi-axis servo system, mechanical resonance and control parameter self-tuning strategy.

Ming Yang (M'14) received the B.S. and M.S. and Ph.D. degrees in Electrical Engineering from Harbin Institute of Technology, Harbin, China, in 2000, 2002 and 2007, respectively.

In 2004, he joined the Department of Electrical Engineering, HIT as a Lecturer, where he has been a Professor of Electrical Engineering since 2015. From 2009 to 2012, he was a Postdoctoral Fellow in Shanghai STEP Electric Corporation. He has authored more than 40 technical papers published in journals and conference proceedings. He is the holder of fourteen Chinese patents. His current major research interests include PMSM servo system, predictive current control and mechanical resonance suppression.

Jiang Long received the M.S. degree in power electronics and electrical drives, in 2015, from the Harbin University of Science and Technology, Harbin, China. He is currently working towards Ph.D. degree in power electronics and electrical drives in the School of Electrical Engineering and Automation of Harbin Institute of Technology.

His current research interest focuses on PMSM servo system, predictive current control and parameter identification.

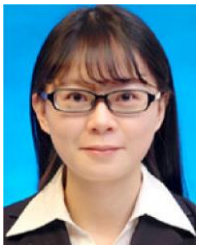

Kun Hu received the B.S. degree in electrical engineering in 2016 from Harbin Institute of Technology, Harbin, China, where she is currently working toward the M.S. degree in power electronics and electrical drives in the School of Electrical Engineering and Automation.

Her current research interests include the electrical engineering and motion control.

Dianguo Xu (M'97–SM'12–F'17) received the B.S. degree in Control Engineering from Harbin Engineering University, Harbin, China, in 1982, and the M.S. and Ph.D. degrees in Electrical Engineering from Harbin Institute of Technology, Harbin, China, in 1984 and 1989, respectively.

In 1984, he joined the Department of Electrical Engineering, HIT as an assistant professor. Since 1994, he has been a professor in the Department of Electrical Engineering, HIT. He was the Dean of School of Electrical Engineering and Automation, HIT from 2000 to 2010. He is now the Vice President of HIT. His research interests include renewable energy generation, power quality mitigation, sensorless motor drives, and high performance servo system.

Dr. Xu is a Fellow of IEEE, and an Associate Editor of the IEEE TRANSACTIONS ON INDUSTRIAL ELECTRONICS.

Frede Blaabjerg (S'86–M'88–SM'97–F'03) was with ABB-Scandia, Randers, Denmark, from 1987 to 1988. He received the Ph.D. degree in electrical engineering from Aalborg University, Aalborg, Denmark, in 1992.

He became an Assistant Professor in 1992, an Associate Professor in 1996, and a Full Professor of power electronics and drives in 1998, Aalborg University. His current research interests include wind turbines, PV systems, reliability, harmonics, and adjustable speed drives.

Dr. Blaabjerg received 15 IEEE Prize Paper Awards, the IEEE PELS Distinguished Service Award in 2009, the IEEE William E. Newell Power Electronics Award 2014, and the Villum Kann Rasmussen Research Award 2014. He was an Editor-in-Chief of the IEEE TRANSACTIONS ON POWER ELECTRONICS from 2006 to 2012. He has been a Distinguished Lecturer for the IEEE Power Electronics Society from 2005 to 2007 and for the IEEE Industry Applications Society from 2010 to 2011. He was nominated in 2014 by Thomson Reuters to be between the most 250 cited researchers in engineering in the world.